Mon. Not. R. Astron. Soc. **000**, 1–15 (2021) Printed 22 July 2022 (MN LATEX style file v2.2)

The recurrent nova V3890 Sgr: a near-infrared and optical study of the red giant component and its environment

B. Kaminsky[1⋆], A. Evans[2]†, Ya. V. Pavlenko[1,3,4], C. E. Woodward[5]‡, D. P. K. Banerjee[6], R. D. Gehrz[5], F. Walter[7], S. Starrfield[8], I. Ilyin[9], K. G. Strassmeier[9], R. M. Wagner[10,11]

[1] *Main Astronomical Observatory, Academy of Sciences of the Ukraine, Golosiiv Woods, Kyiv-127, 03680 Ukraine*
[2] *Astrophysics Group, Lennard Jones Laboratory, Keele University, Keele, Staffordshire. ST5 5BG, UK*
[3] *Centre for Astrophysics Research, University of Hertfordshire, College Lane, Hatfield, AL10 9AB, UK*
[4] *Nicolaus Copernicus Astronomical Center, ul. Rabianska 8, 87-100 Toruń, Poland*
[5] *Minnesota Institute for Astrophysics, School of Physics & Astronomy, 116 Church Street SE, University of Minnesota, Minneapolis, MN 55455, USA*
[6] *Physical Research Laboratory, Navrangpura, Ahmedabad, Gujarat 380009, India*
[7] *Department of Physics & Astronomy, Stony Brook University, Stony Brook, NY, 11794-3800, USA*
[8] *School of Earth and Space Exploration, Arizona State University, Box 871404, Tempe, AZ 85287-1404, USA*
[9] *Leibniz-Institut für Astrophysik Potsdam (AIP), An der Sternwarte 16, D-14482 Potsdam, Germany*
[10] *Department of Astronomy, The Ohio State University, 140 W. 18th Avenue, Columbus, OH 43210, USA*
[11] *Large Binocular Telescope Observatory, 933 North Cherry Avenue, Tucson, AZ 85721, USA*

Version of 22 July 2022

ABSTRACT

We present an analysis of the red giant component of the recurrent nova V3890 Sgr, using data obtained before and after its 2019 eruption. Its effective temperature is $T_{\rm eff}$ = 3050±200 K for $\log g = 0.7$, although there are modest changes in $T_{\rm eff}$. There is an overabundance of both carbon (0.20 ± 0.05 dex) and sodium (1.0 ± 0.3 dex) relative to their solar values, possibly the result of ejecta from the 1990 nova eruption being entrained into the red giant photosphere. We find $^{12}{\rm C}/^{13}{\rm C} = 25 \pm 2$, a value similar to that found in red giants in other recurrent novae. The interpretation of the quiescent spectrum in the 5–38 μm region requires the presence of photospheric SiO absorption and cool ($\sim$ 400 K) dust in the red giant environment. The spectrum in the region of the Na I D lines is complex, and includes at least six interstellar components, together with likely evidence for interaction between ejecta from the 2019 eruption and material accumulated in the plane of the binary. Three recurrent novae with giant secondaries have been shown to have environments with different dust content, but photospheres with similar $^{12}{\rm C}/^{13}{\rm C}$ ratios. The SiO fundamental bands most likely have a photospheric origin in the all three stars.

Key words: circumstellar matter – stars: AGB and post-AGB — stars: abundances — stars: individual (V3890 Sgr) — novae: cataclysmic variables — infrared: stars

1 INTRODUCTION

Novae are semi-detached binary systems in which a cool star fills its Roche lobe. Material from the cool star (the secondary) flows through the inner Lagrangian point and spirals onto the surface of a white dwarf (WD) via an accretion disc (AD). In time, the base of the accreted layer becomes degenerate, and a thermonuclear runaway (TNR) occurs on the WD surface. This results in the explosive ejection of up to $\sim 10^{-4}\,{\rm M}_{\odot}$ of material at several 100s to several 1000s of $\,{\rm km\,s^{-1}}$: a nova eruption has occurred.

After the eruption, mass transfer resumes and in time ($\lesssim 10^6$ yrs), conditions again become suitable for another nova eruption. All novae are therefore recurrent, but those that repeat on a human timescale ($\lesssim$100 yrs) are known as Recurrent Novae (RNe; see Evans et al. 2008; Schaefer

⋆ E-mail: bogdan@mao.kiev.ua
† Corresponding author. Email: a.evans@keele.ac.uk
‡ Visiting Astronomer at the Infrared Telescope Facility, which is operated by the University of Hawaii under contract 80HQTR19D0030 with the National Aeronautics and Space Administration.

2010, for reviews), as opposed to the more leisurely Classical Novae (CNe).

While several hundred CNe are known, only about a dozen RNe are known (see Anupama 2008, for a summary). A CN loses its "classical" status if it is seen to erupt again within less than a few decades of eruption: undoubtedly there are systems that are RNe, as normally defined, masquerading as CNe (see, e.g. Pagnotta & Schaefer 2014, and references therein). Indeed, it has been suggested (Pagnotta & Schaefer 2014; Della Valle & Izzo 2020) that as many as 30% of CNe may be recurrents.

RNe are of particular interest in that the WD in these systems are thought to be close to the Chandrasekhar limit (Starrfield, Iliadis & Hix 2016), and potentially therefore progenitors of Type Ia supernovae. The latter of course are a crucial tool in the determination of large-scale cosmic structure (Reiss et al. 1998; Perlmutter et al. 1999), so an understanding of RNe has wide application.

In this paper we report on the analysis of the optical, near-infrared (NIR) and mid-IR spectra of the RN V3890 Sgr, obtained while it was in quiescence, both before and after its 2019 eruption (see Section 2). A discussion of the NIR spectra obtained during the 2019 eruption will be presented elsewhere (Evans et al. 2022b).

2 THE RN V3890 Sgr

The RN V3890 Sgr has undergone eruptions in 1962, 1990 (e.g., Anupama 2008), and most recently on 2019 Aug 27.87 (Pereira 2019). The orbital period of V3890 Sgr is listed by Schaefer (2009) as 519.7 ± 0.3 days, with semi-major axis $362\,\mathrm{R}_\odot$. However, a more recent analysis, using extensive spectroscopic and photometric data (Mikołajewska et al. 2021), gives the orbital period as 747.6 days with binary separation $a \sin i \simeq 430\,\mathrm{R}_\odot$, where i is the binary inclination. Mikołajewska et al. (2021) found that $i \simeq 68^\circ$, so the system is not eclipsing. While these orbital parameters are consistent with a red giant (RG) that fills (or almost fills) its Roche lobe, there seems to be no clear evidence in the visual light curve that can clearly be attributed to ellipsoidal variations (Mikołajewska et al. 2021). Indeed data from the OGLE survey (Soszynski et al. 2013) suggest that the light variations of V3890 Sgr can be quite erratic.

Darnley et al. (2012) have discussed the quiescent optical and NIR colours of V3890 Sgr. Its optical properties suggest a sub-giant secondary, while its NIR colours are more consistent with a RG secondary. Darnley et al. suggest that this discrepancy indicates a high accretion rate and hence high luminosity AD, especially if the binary system is close to face-on; however this conflicts with the inclination determined by Mikołajewska et al. (2021). Its quiescent K_s magnitude and orbital period place it together with RS Oph (although Darnley et al. 2012, use the Schaefer (2009) period). Its rate of decline from maximum, and its high ejection velocities, during eruption (see, e.g., Evans et al. 2022b) also place it in Darnley et al.'s "RG-Novae" category.

The mass ratio is $q = 0.78 \pm 0.05$ for V3890 Sgr (Mikołajewska et al. 2021). Using the dependence of $\log g$ on q (see Figure 1 of Pavlenko et al. 2020b), this translates to $\log g = 0.72 \pm 0.02$ for the RG in V3890 Sgr. We assume $\log g = 0.7$ here, although the calculated spectral energy distribution (SED) is not sensitive to the value of $\log g$ assumed.

The secondary star in V3890 Sgr has been variously classified as M8 III (Williams et al. 1991) and M5 III (Harrison, Johnson & Spyromilio 1993; Anupama & Mikołajewska 1999); the observations on which these classifications were based were carried out before (Williams et al. 1991) and after (Harrison et al. 1993; Anupama & Mikołajewska 1999) the 1990 eruption. The effective temperature corresponding to these classifications ranges from $T_{\rm eff} \sim 3100$ K to ~ 3400 K (see, e.g., van Belle et al. 2021).

The reddening to V3890 Sgr has been discussed in detail by Page et al. (2020), who found that various authors have deduced $E(B-V)$ values in the range 0.46–1.1, depending on the method used. Page et al. also found that the ultraviolet (UV) data are best dereddened with a SMC extinction law (Prévot et al. 1984), which is steeper in the UV than the "conventional" Galactic extinction law and lacks the 2175Å extinction bump. The SMC law is required to give a satisfactory account of the "2175Å" bump, and leads to a high UV flux. A reddening value $E(B-V) = 0.59$, based on an analysis of the interstellar Na I D lines from CHIRON spectra (see below), was obtained by Munari & Walter (2019). In view of the various uncertainties we shall treat the reddening as a parameter to be determined as part of the fitting routine. However we use a conventional Galactic extinction law (Cardelli, Clayton & Mathis 1989).

3 OBSERVATIONS OF V3890 SGR IN QUIESCENCE

V3890 Sgr was observed both before and after the 2019 eruption, at optical, NIR and mid-IR wavelengths, covering the wavelength range 4070Å–38 μm. None of the observations are contemporaneous. We summarise the observations below, and in Table 1. In order to model the SED of the RG, we must determine whether the RG photosphere is irradiated by the WD. Using the ephemeris of Mikołajewska et al. (2021), we find the orbital phases given in Table 1; phase zero is when the RG component is at inferior conjunction.

3.1 Before: *Spitzer* IRS

V3890 Sgr was observed on 2007 October 11.27 UT with the *Spitzer Space Telescope* (Werner et al. 2004; Gehrz et al. 2007) InfraRed Spectrograph (IRS; Houck et al. 2004) as part of the *Spitzer* programme PID 40060 (P.I. A. Evans). The spectrum was retrieved from the *Combined Atlas of Sources with Spitzer IRS Spectra* (CASSIS; Lebouteiller et al. 2011), and is shown in Fig. 1. The spectrum is almost featureless. The only possible feature is the SiO fundamental in absorption (see Fig. 1), which was also seen in the *Spitzer* IRS spectrum of the RNe T CrB (Evans et al. 2019) and RS Oph (Rushton et al. 2022). The V3890 Sgr Spitzer data were obtained at orbital phase 0.52, when the WD was in front of the RG; irradiation effects may therefore be important in this case.

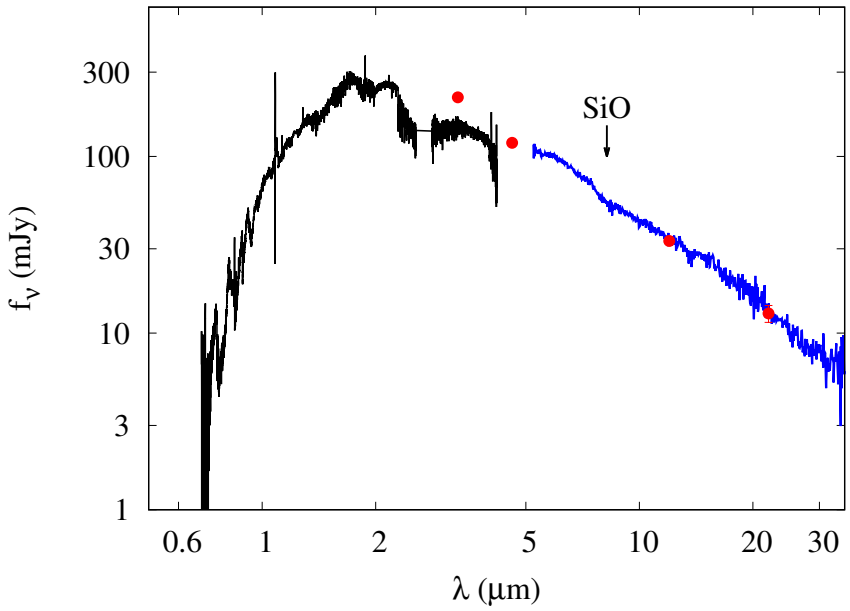

Figure 1. Quiescent spectrum of V3890 Sgr, using post-2019-eruption ground-based data from 2020 June 6 (black), pre-eruption *Spitzer* IRS data (blue; obtained in 2007 October) and pre-eruption *WISE* survey data (red points; obtained in 2010 March). The sharp feature just longward of 1 μm is He I $\lambda = 1.083\,\mu$m, that at 1.8 μm is Pa-α. The location of the SiO fundamental at 8 μm is indicated. See text for details

Table 1. Dates and orbital phases for the observations.

Facility	Instrument	Wavelength Range	Resolution $\lambda/\delta\lambda$	UT Date YYYY-MM-DD.DD	JD – 2450000	Orbital phase*
			Before 2019 eruption			
Spitzer	IRS	5–38 μm	~ 100	2007-10-11.27	4384.77	0.52
*WISE***	—	3.6–22 μm	~ 1	2010-03-27.60	5283.10	0.72
″	—	3.6–22 μm	~ 1	2010-09-25.85	5465.35	0.97
SMARTS	CHIRON	4071–8908Å	27800	2018-05-13.35	8251.85	0.69
SMARTS	CHIRON	4071–8908Å	27800	2018-05-16.32	8254.82	0.69
			After 2019 eruption			
SMARTS†	CHIRON	4070 – 8907Å	78000	2019-08-29.06	8724.56	0.33
SMARTS†	CHIRON	4070 – 8907Å	27800	2019-09-03.03	8730.53	0.34
SMARTS‡	CHIRON	4070 – 8907Å	27800	2019-09-16.02	8742.52	0.35
SMARTS‡	CHIRON	4070 – 8907Å	27800	2019-09-26.02	8752.52	0.36
IRTF	SpeX	0.7–2.6 μm	750	2020-05-20.53	8990.00	0.68
IRTF	SpeX	0.7–4.2 μm	1200	2020-06-06.56	9007.06	0.70
LBT	PEPSI	4219–7426Å	130000	2020-06-10.27	9010.77	0.71
IRTF	SpeX	0.7–2.6 μm	1200	2021-05-25.48	9360.02	0.18
IRTF	SpeX	0.7–2.6 μm	1200	2021-07-07.40	9402.90	0.23

*From the ephemeris of Mikołajewska et al. (2021). Phase zero is when the RG component is in front of the WD
** *WISE* photometry was taken over the period 2001 March 27 – September 26. Ssee text for details.
†These spectra were taken *close to the peak* of the 2019 eruption.
‡These spectra were taken during the decline of the 2019 eruption.

3.2 WISE

V3890 Sgr was detected in the Wide-field Infrared Survey Explorer survey (*WISE*; Wright et al. 2010) in 2010 March and September. *WISE* data for CNe and RNe were presented by Evans et al. (2014). The fluxes for V3890 Sgr are listed in Evans et al. but are given here (Table 2) for completeness, and plotted in Fig. 1.

While Evans et al. (2014) stated that *WISE* data are consistent with a blackbody photosphere at 2310 K, with no evidence of line or dust emission, the blackbody fit was not

Table 2. Fluxes for V3890 Sgr from the *WISE* survey (Evans et al. 2014).

WISE band	λ (μm)	Flux density (mJy)	Flux error (mJy)
$W1$	3.3	216	5
$W2$	4.6	119	2
$W3$	12	33.2	0.6
$W4$	22	12.93	1.42

entirely satisfactory. This is clearly because the *WISE* data cover only the Rayleigh-Jeans tail of the stellar photosphere and do not capture the intricacies of the stellar emission (see Fig. 1).

The *WISE* data were obtained over the period 2010 March 27 – September 26. However the survey passes were concentrated in ~ 1 day-long "bursts", around MJD 55282.5 and MJD 55464.0; the mean MJD values are 55282.60 (2010 March 27.60: "epoch 1") and 55464.85 (2010 September 25.85: "epoch 2"), the values entered in Table 1. The weighted mean *WISE* magnitudes for these two epochs are $W1 = 7.842 \pm 0.025$, $W2 = 7.841 \pm 0.020$ (epoch 1) and $W1 = 7.935 \pm 0.030$, $W2 = 7.952 \pm 0.023$ (epoch 2) respectively. The mean values of $W1$ and $W2$ for these two epochs differ significantly at better than the 0.5% level. This difference can be attributed to the fact that epoch 1 data were obtained at quadrature (when any ellipsoidal effect would have been at its greatest extent), while epoch 2 data were obtained when the RG was in front of the WD (see Table 1, but also Section 2).

3.3 Before and after: SMARTS

V3890 Sgr was observed as part of the Stony Brook/SMARTS Nova program (Walter et al. 2012), on 2018 May 13.35 and 16.32 (both UT), with the CHIRON echelle spectrograph. The spectra covered the wavelength range 4071Å–8908Å, at resolution $R = \lambda/\delta\lambda = 27800$. In this paper we discuss mainly the 2018 May 16 pre-2019 spectrum; similar data were also obtained on 2019 September 16.02 and 26.02 (both UT), after the 2019 eruption. High resolution ($R = 78000$) data, covering the same wavelength range, were obtained on 2019 August 29 close to the peak of the 2019 eruption, and are also discussed here.

The data were retrieved from the SMARTS Nova program website[1]. These data were obtained at a variety of orbital phases, as detailed in Table 1.

3.4 After: IRTF

NIR spectra of V3890 Sgr were obtained on 2020 May 20.53 and 2021 May 25.48 UT with the infrared spectrograph SpeX (Rayner et al. 2003) on the NASA Infrared Telescope Facilty IRTF. Full details of the data reduction are given in Evans et al. (2022b) and are not repeated here. In each case the spectra showed essentially the "normal" SED of the RG component, with few emission lines superimposed. By these dates the system had essentially returned to quiescence (Woodward et al. 2019). The spectrum for 2020 June 6 is included in Fig. 1, to give an overall impression of the SED in quiescence.

As noted in Table 1, the post-eruption IRTF data were obtained at two distinct orbital phases. These two spectra are shown in Fig. 2, together with the spectra of two M giants (EU Del, M6, and HD175865, M5) from the IRTF Spectral Library (Rayner, Cushing & Vacca 2009). The data for the two M giants have been reddened by $E(B-V) = 0.4$, to enable comparison with the observed spectrum of V3890 Sgr.

3.5 After: PEPSI

High spectral resolution ($R = 120000$) optical observations of V3890 Sgr in quiescence were obtained with the Potsdam Echelle Polarimetric and Spectroscopic Instrument (PEPSI; Strassmeier et al. 2015) on the Large Binocular Telescope (LBT; Hill et al. 2012) on 2020 June 10.2653 UT with the 200 μm fibre using both apertures of the twin 8.4-m mirrors. Two sets of blue/red-arm cross-dispersing (CD) combinations were used, III/V (4800-5441 Å/6278-7419 Å) and II/IV (4265-4800 Å/5441-6278 Å), with an integration time for each pair of 40 minutes $\times 2$ exposures. The average seeing, as measured from the peripheral wavefront sensors, was $1\farcs01$ and V3890 Sgr was near 2.34 airmasses at the start of the observation. The spectrophotometric standard 58 Aql was also observed with a similar instrumental setup. The raw CD data were processed through the standard PEPSI pipeline (SDS4PEPSI version: 20210715), in which the barycentric wavelengths were corrected for a -8912.305 m s^{-1} radial velocity to the barycenter of the Solar System. The various CD exposures were combined with a weighted average, and then flux normalized (dimensionless units).

4 MODELLING THE RG SPECTRUM

To fit the observed SED over a wide spectral range we used classical model atmospheres computed in local thermodynamic equilibrium (LTE; Pavlenko 2013). The contributions of selected diatomic molecules and H_2O to the model SED in the wavelength range 0.7 μm–2.6 μm are shown in Fig. 3, in which each model curve includes the contributions of the molecule and H^- only. The H^- is responsible for the peak at $\sim 1.6\,\mu$m.

4.1 Synthetic spectra and model atmospheres

To generate synthetic spectra, we used the SAM12 model atmosphere code (Pavlenko, Yurchenko & Tennyson 2020a; Pavlenko et al. 2020b, and references therein). The procedure for computing synthetic spectra is described in Evans et al. (2019), which also gives sources for the molecular line lists. Line profiles were computed using Voigt profiles, and damping constants were taken from the line list databases, or computed in the Unsöld (1927) approximation. Synthetic spectra were computed in wavelength steps of 0.025 Å (0.025Å to 1Å for the Spitzer data). We determined the value of the turbulent velocity (V_t) simultaneously with carbon isotope ratio for all individual spectra. Also, our fitting

[1] http://www.astro.sunysb.edu/fwalter/SMARTS/NovaAtlas

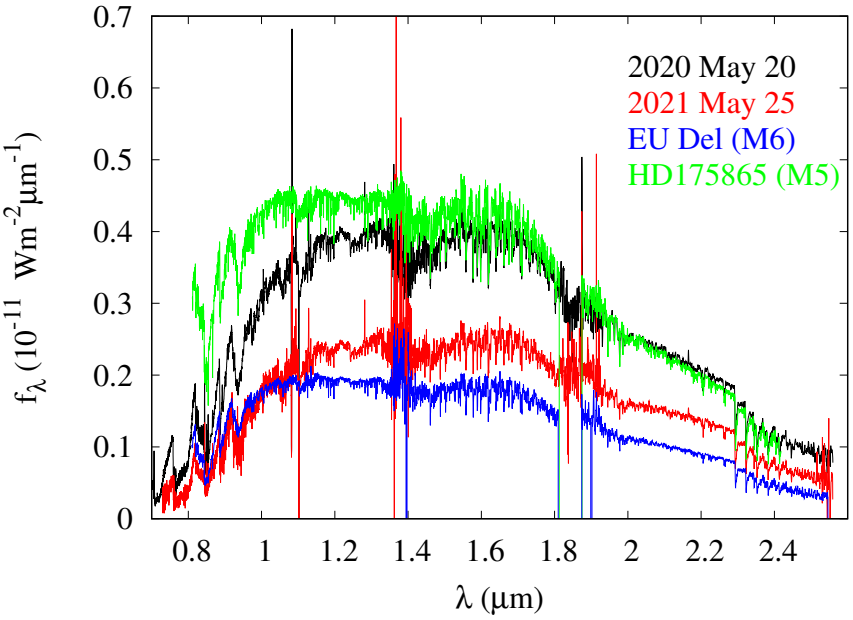

Figure 2. The two IRTF spectra obtained post outburst. Also shown are the spectra of EU Del (M6 IIII) and HD175865 (M5 III) from the IRTF Spectral Library (Rayner et al. 2009). EU Del and HD175865 have been reddened by $E(B-V) = 0.4$ (see text).

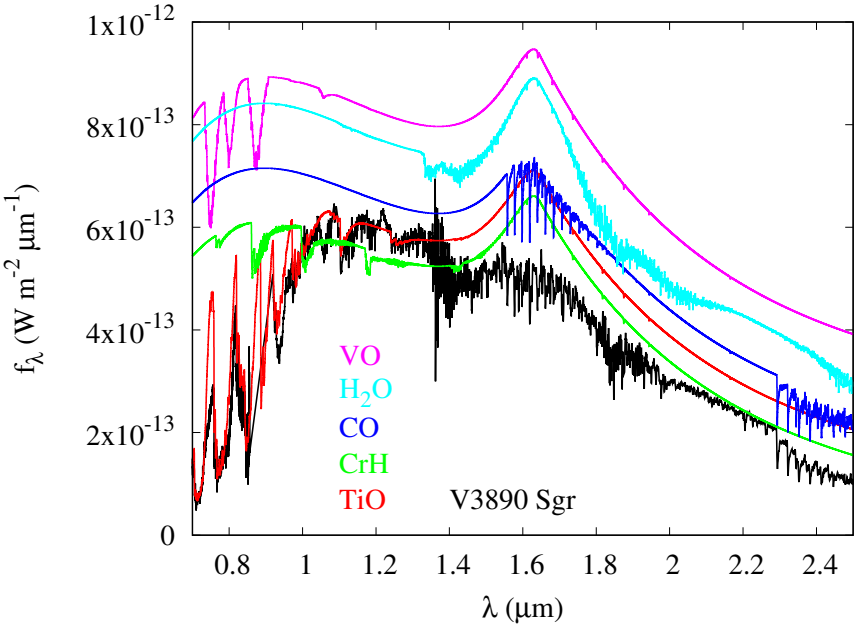

Figure 3. Identification of the H_2O bands and the main diatomic molecules that contribute to the SED of the RG in V3890 Sgr; the individual molecular contributions have been displaced vertically by arbitrary amounts for clarity. Diatomics that have minimal effect on the spectrum (such as FeH) are not shown. The spectrum of V3890 Sgr is from 2020 May 20 and has been dereddened.

procedure did not reveal any notable rotational velocities[2] $v \sin i$; therefore the theoretical spectra were convolved with a pure Gaussian profile in order to model the instrumental broadening.

We computed a grid of RG model atmospheres for the effective temperatue range $T_{\rm eff}$ 2800–3700 K in steps of 100 K and having solar (Asplund 2009) abundances; $\log g$ was taken to be 0.7 for all models.

The best fit to the observed spectra was achieved by the χ^2 procedure described in Pavlenko (2014). We give a few details here to aid understanding of our procedure. As part of the fit, the function

[2] Here i is the inclination of the RG rotation axis, not the orbital inclination.

$$S = \sum_{i=1}^{N} s_i^2 \quad (1)$$

is minimised, where $s_i = |F_i^{\rm obs} - F_i^{\rm comp}|$; $F_i^{\rm obs}$ and $F_i^{\rm comp}$ are the observed and computed fluxes, respectively, and N is the number of the wavelengths points used in the minimisation procedure. Three parameters were used in our minimisation procedure: the heliocentric velocity of V3890 Sgr in $\rm km\,s^{-1}$, the flux scale normalisation parameter, and the full width at half maximum (FWHM) used for the smoothing Gaussian. They were determined for every fitted spectral range. In our analysis we omitted some spectral ranges that contained artifacts provided by strong noise, telluric absorption, bad pixels, etc. The minimisation sum S was computed on a 3D grid of radial velocity sets, flux normalisation factors, and FWHM parameters. Errors in the fit were evaluated as $\Delta S = \sum s_i/N$.

The data were dereddened by $E(B-V) = 0.4, 0.5, 0.6$ (cf. Mikołajewska et al. 2021) prior to fitting.

5 RESULTS

5.1 The IRTF data

5.1.1 SED, $T_{\rm eff}$ and abundances

While our approach is simplified, we obtained good fits to the NIR spectra using solar abundances, with the exception of carbon (see Figs 4 and 5). We adopt[3] [C] = $+0.20 \pm 0.05$ dex to reduce the effect of absorption by the water and TiO molecular bands, which are too strong if the solar abundance of carbon is assumed (see Fig. 5). This is because the additional carbon captures oxygen, resulting in a decrease in the abundance of H_2O and TiO. The only exception to the quality of the fit is in the 1.00–1.45 μm region, where we see a significant overestimation of the opacity in the theoretical model (note that the theoretical curve falls below the observed spectrum). All four IRTF spectra yield the same discrepancy in this wavelength region, even though the spectra were all obtained approximately at quadrature (see Table 1). In general, it is found that theoretical fluxes are larger than observed due to a lack of opacity in the models. In the case of the IRTF data on V3890 Sgr, however, we see the opposite effect: in our model the opacity is *overestimated.* Alternatively the temperatures at the depths at which the 1.00–1.45 μm flux originates differ from our models. This undoubtedly points to the limitations of the model used, and that a more sophisticated model than that used here is needed for such a complex object.

The values of $T_{\rm eff}$ and $E(B-V)$ for all four dates, obtained from the fitting procedure, are given in Table 3, and the best fit for 2020 May 20 is shown in Fig. 4. From Table 3 one may see that we obtained two different values of $T_{\rm eff}$, namely 3000 K and 3100 K. These values do not differ within the uncertainty of $\pm$200 K, and both values were found for dates with similar orbital phase ($\simeq 0.7$ and $\simeq 0.2$) so any difference cannot be due to irradiation effects. We adopt $T_{\rm eff} = 3050 \pm 200$ K from fitting the NIR data.

We obtained the same solution for the reddening ($E(B-V) = 0.4$) for all four dates, and this value is at the lower end of the range given in Page et al. (2020). Our low value of $E(B-V) = 0.4$ is based on fitting the SED, but according to Mikołajewska et al. (2021), the SED of V3890 Sgr may be affected by additional flux from the AD. Such addional flux, which increases to the blue, provides partial compensation for the reddening, and leads to a lower $E(B-V)$ value.

There are a number of strong absorption lines in the NIR spectrum of V3890 Sgr. Some of the stronger atomic features are identified in Fig. 5. In general, the determination of atomic abundances by fitting the stronger lines in low resolution spectra is affected by a number of uncertainties (such as non-LTE, saturation of lines, etc.). Nevertheless we have determined the abundances of a number of species by fitting observed line profiles.

In general the abundances are close to solar, but there is an overabundance of sodium relative to solar, by a factor $\sim 1.0 \pm 0.3$. Since the NIR Na I lines used in the analysis are not resonance lines, we are confident that they can not be interstellar. Such an overabundance is not unexpected as a result of the TNR (Starrfield et al. 2009, 2020). However, as discussed by Pavlenko et al. (2020b), the extent to which the TNR products pollute the RG photosphere is unclear.

5.1.2 The $^{12}C/^{13}C$ ratio

We have determined the ^{12}C/^{13}C ratio for four separate datasets after V3890 Sgr had returned to quiescence. These values, together with the determined values of $T_{\rm eff}$ and the microturbulent velocity V_t, are summarised in Table 3.

The fit of our synthetic spectra across the first overtone CO bands to the 2020 May IRTF spectrum is shown in Fig. 6; details of our procedure are given in Pavlenko et al. (2020b).

We have now determined the ^{12}C/^{13}C ratio for the RG components of three RNe, as summarised in Table 4. These values all seem to be consistent with that expected (~ 20) after first dredge-up, for stars with initial masses $\gtrsim 2\,{\rm M}_\odot$ (see, e.g. Karakas & Lattanzio 2014), and are significantly lower than the solar value of ~ 90. However as with the sodium abundance, the RG photosphere may be polluted by the products of the 1990 TNR and the measured ^{12}C/^{13}C ratio in these systems may reflect this process.

5.1.3 SiO first overtone absorption

The spectrum obtained on 2020 June 26 extends to 4.2 μm, and clearly shows the presence of first overtone SiO in absorption (see Fig. 7). A fit of the model atmosphere already used to model the NIR data to this spectral range suggests that the Si abundance is essentially solar ([Si] $= 0.0 \pm 0.5$ in Fig. 7); the uncertainty in the abundance of Si is greater than it is for C because of the noisier data in the 4 μm band. This has implications for the modelling of the SiO fundamental (see Section 5.3.3 below).

5.2 The CHIRON and PEPSI optical spectra

In this subsection we discuss the CHIRON and PEPSI spectra, and consider what they imply for the wind and environment of the RG.

[3] [C] = [C/Fe] = $({\rm C/Fe})_{\rm V3890\ Sgr} - ({\rm C/Fe})_\odot$.

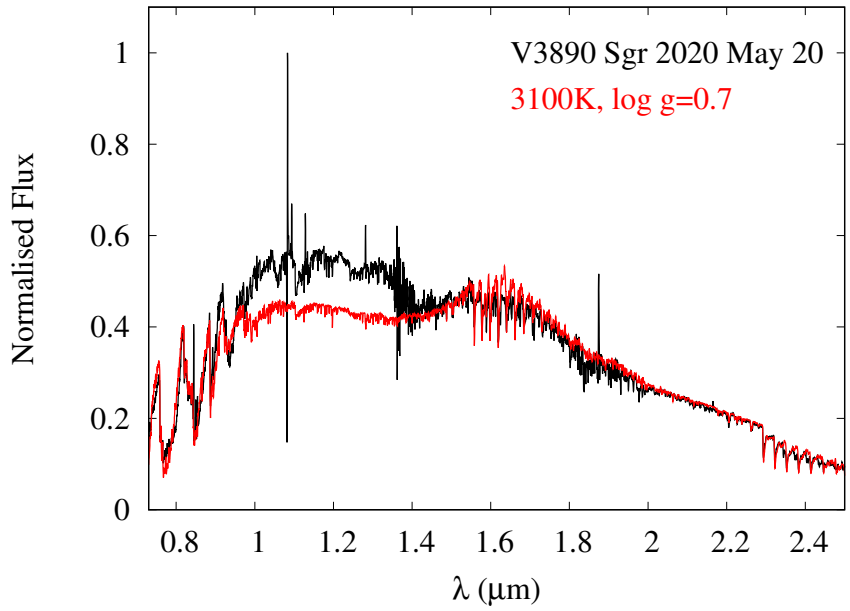

Figure 4. Model fits (red) to the dereddened SED of V3890 Sgr (black) on 2020 May 20 (orbital phase 0.68). The model atmosphere has $T_{\rm eff}$ = 3100 K, $\log g = 0.7$; solar abundances are assumed, except for [C] = 0.2. The best fit is for $E(B-V) = 0.4$. The flux scale has been normalised so that the maximum f_λ in the observed spectrum has value unity.

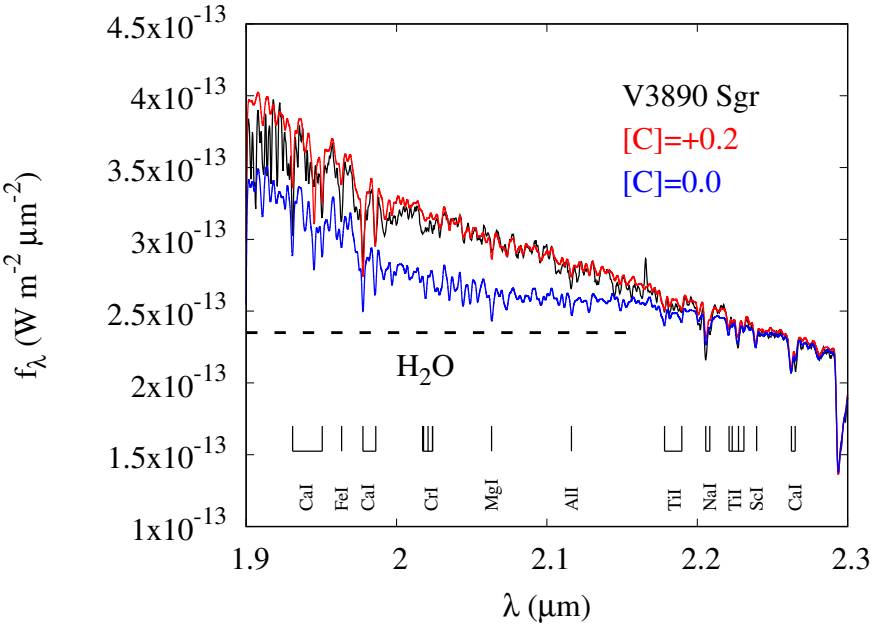

Figure 5. Fit to the dereddened NIR SED of V3890 Sgr for 2020 May 20; atomic features are identified. Red curve is a synthetic spectrum with $T_{\rm eff}$ = 3100 K, $\log g = 0.7$ and [C] = +0.2; blue curve has [C]=0.0. The broken line indicates the extent of the water band. The first overtone ^{12}CO bandhead is just visible at 2.29 μm.

5.2.1 CHIRON

One day after the 2019 eruption (2019 Aug 28), the flux has clearly increased significantly, but only interstellar Na I D lines appear to be present in this region (Fig. 8 top left). At high resolution, at least six interstellar features are evident, all at positive radial velocity. The radial velocity of the main interstellar Na I feature is the same as that of the interstellar K I resonance doublet.

The first post-outburst low resolution spectrum was obtained on 2019 September 3. While the flux has decreased by a factor of five, only the interstellar lines are present, shown in red in the top left panel of Fig. 8. By 2019 September 15, the flux had decreased by a further factor of seven, and broad blue-shifted Na I emission from the expanding ejecta

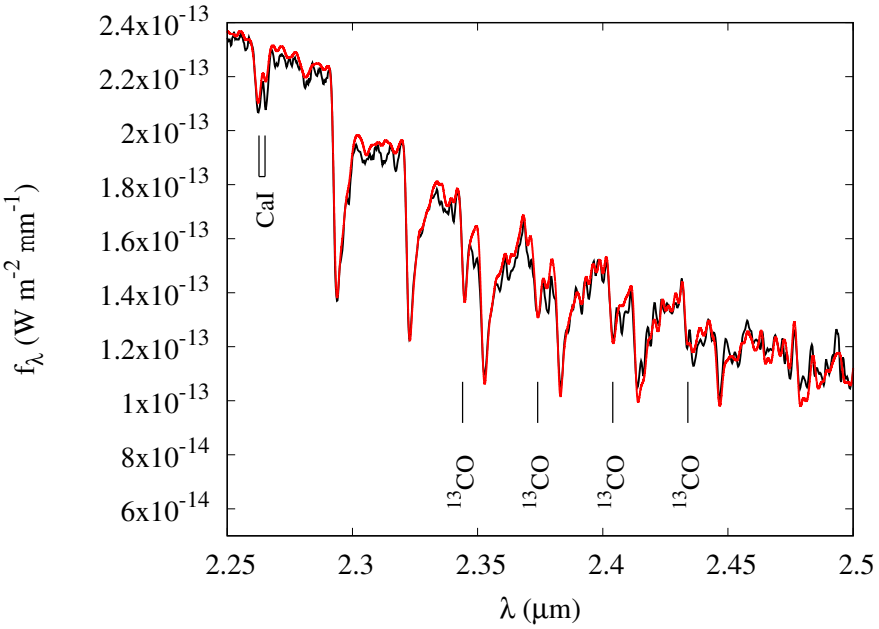

Figure 6. Best fit to the observed first overtone CO bands in V3890 Sgr. Data from 2020 May have been dereddened. The ^{13}CO band heads and Ca I are identified.

Table 3. Determination of the $^{12}C/^{13}C$ from four separate datasets. R is the effective spectral resolution.

Date YYYY-MM-DD	$T_{\rm eff}$ (K)	V_t ($\rm km\,s^{-1}$)	$^{12}C/^{13}C$	$E(B-V)$	R	Orbital phase
2020-05-20	3100	2.2	27	0.4	1050	0.68
2020-06-06	3000	2.2	24	0.4	1300	0.70
2021-05-25	3000	2.2	21	0.4	1300	0.18
2021-07-07	3100	2.2	27	0.4	1300	0.23

appears. Possibly this component was present, but obscured, at earlier times because of the high outburst flux. On 2019 September 26, the flux had decreased by a further factor of three, and the broad Na I emission features had become relatively stronger.

In the top right panel of Fig. 8, the black/green curves correspond to the black/green curves in the top left panel, but now the pre-outburst spectrum (magenta) from 2018 May is included. The flux level in the latter is some 23 times lower than the 2019 September 26 value (green). The wings of the broad Na I emission features arising from the ejecta (green) are clearly present in the 2018 May spectrum. However, as shown in the bottom left panel of Fig. 8, two blue-shifted absorption features are seen superimposed on the broad emission. Of these, one component (the stronger) at 5887.6/5893.5Å (D_2 and D_1 respectively) at radial velocity $-17\,\rm km\,s^{-1}$, the other at 5888.8/5894.7Å has radial velocity $+44\,\rm km\,s^{-1}$. There are weak absorption features in the *post-outburst* high resolution data that correspond to the stronger $-17\,\rm km\,s^{-1}$ component, which we suggest is the wind of the RG. P Cygni profiles may be present as well.

In the bottom left panel of Fig. 8, we show the Na I D lines for 2018 May 16 in velocity space. These data were obtained 18 years after the 1990 outburst, and 1 year before the 2019 outburst. All the above-mentioned features are labelled in the bottom left panel of Fig. 8. Two absorption features have radial velocities $+44\,\rm km\,s^{-1}$ and $-17\,\rm km\,s^{-1}$. These lines are weak one month after the (2019) outburst, but much stronger in the pre- and post-outburst PEPSI data. The profiles of the Na I D lines, and the changes therein, are likely due to the complex interactions between the RG wind and material ejected in the 2019 and previous eruptions, and material remaining from the common envelope phase of evolution (see Booth, Mohamed & Podsiadlowski 2016).

The bottom right panel of Fig. 8 shows the permitted lines of He I 5875Å, 6678Å, and the forbidden [O III] 5006Å line before the 2019 eruption. This is included here for comparison with Fig. 9 below.

5.2.2 PEPSI

Segments of the 2020 Jun 10.27 UT spectra are presented in Fig. 9. These data span a gap in the Mikołajewska et al. (2021) spectral coverage, being at a phase of 0.71, and were obtained with higher resolving power ($R = 130,000$), enabling study of subtle structures in various line regions. The PEPSI spectra show a range of features, including emission lines of H I, He I, [O III], O I, and weaker emission from N II and Ca I. The He II 4686Å and the [N II] 6583Å lines are not detected within the SNR-limit of the spectrum. The Na I $D_{1,2}$ region is complex, with many absorption components

Table 4. The $^{12}C/^{13}C$ ratio, dust temperatures, and SiO in the RG components of RNe.

RN	Dust	SiO	$^{12}C/^{13}C$	Reference
RS Oph	600 ± 100 K silicate			Evans et al. (2007b)
	400–500 K silicate			Rushton et al. (2010)
			16 ± 3	Pavlenko et al. (2010)
		Absorption: photospheric		Rushton et al. (2022)
T CrB	None	Absorption: photospheric	10 ± 2	Evans et al. (2019), but see Evans et al. (2022a) for important erratum
V3890 Sgr	400 K; composition indeterminate	Absorption: photospheric	25 ± 2	This work

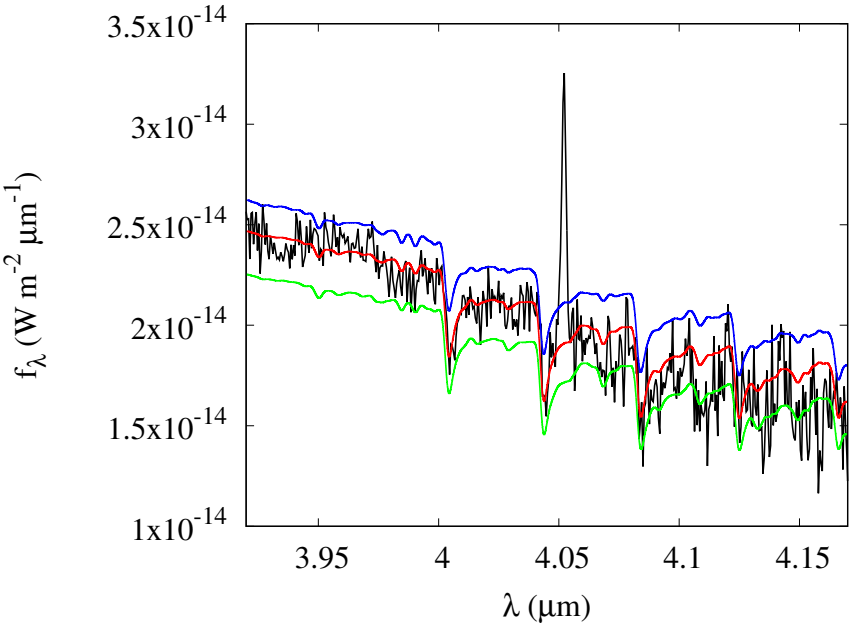

Figure 7. Fit of model atmospheres having various Si abundances to the first overtone SiO bands. Black curve: V3890 Sgr, dereddened as discussed in text. Red curve: computed first overtone SiO, assuming solar Si abundance. Blue curve: as red curve but with Si abundance [Si] = −0.5. Green curve: as red curve but with Si abundance [Si] = +0.5. Blue and green curves have been displaced upwards and downwards respectively for clarity. The emission feature is H I Brackett α (5–4) at 4.052 μm.

(but note the comment in the caption about the number of distinct absorption systems). The Hα line is the strongest observed line with very broad wings, fit well by a Lorentzian with a double-peaked profile, the red peak being stronger than the blue peak (see Fig. 9 top panel). On the other hand, the Hβ line resembles more a Gaussian in overall line profile shape, with a FWHM of $\sim 165.18\,\mathrm{km\,s^{-1}}$. Both lines have absorption components of their blue wings, with the strongest component blue shifted $\sim -30\,\mathrm{km\,s^{-1}}$ with respect to the binary systemic velocity ($94\,\mathrm{km\,s^{-1}}$, Mikołajewska et al. 2021), while Hα has another component at $\sim 100\,\mathrm{km\,s^{-1}}$. The PEPSI spectrum, together with the CHIRON spectrum from 2020 March 8, clearly demonstrate that this feature was quite strong for at least 94 days, from 2020 March 8 through 2022 Jun 10, before diminishing in intensity 13 days later (see Fig. 7 in Mikołajewska et al. 2021).

Williams et al. (2008) reported transient absorption features, with velocities of a few hundred $\mathrm{km\,s^{-1}}$, in high-resolution ($R = 48000$) optical spectra of CNe shortly after outburst. These features arise in a wide range of heavy elements (e.g., Sc, Ti, V, Cr, Fe), and progressively weaken with a few weeks of the eruption. They suggest that these features arise in material ejected by the secondary, and which pre-dates the nova eruption. The behaviour of the Hβ absorptions in V3890 Sgr is reminiscent of that described by Williams et al., and may arise in the same way.

The broad He I 5875Å, He I 6678Å profiles are symmetric about the systemic velocity, while the forbidden emission line profile [O III] 5006Å line is sharply peaked with a FWHM $\sim 35.28\,\mathrm{km\,s^{-1}}$ (see Fig. 9 middle panel).

The permitted O I 5014Å and adjacent He I 5016Å features are symmetric, with similar integrated line intensities with FWHM $\sim 83.89\,\mathrm{km\,s^{-1}}$ and a narrower FWHM $\sim 56.62\,\mathrm{km\,s^{-1}}$, respectively. The Fe II 5018Å line, seen in other symbiotic spectra (Quiroga et al. 2002), is not detected. The ratio of the integrated [O III] to O I intensity is ~ 1.58.

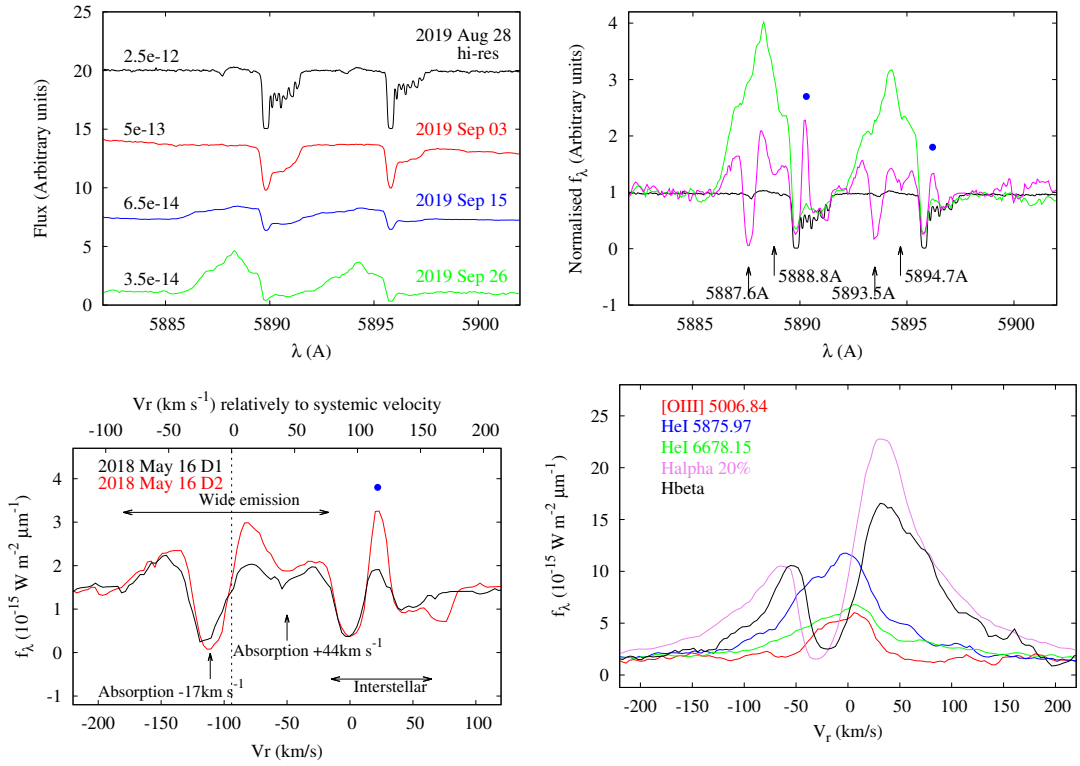

Figure 8. Top left: high resolution spectra of V3890 Sgr in the region of the Na I D lines on the dates indicated. The numbers attached to each spectrum give the flux densities at 5883Å. Top right: post-2019 eruption spectra on the dates indicated; the 2019 August 28 (black) and 2019 September 26 (green) spectra from the left panel are replicated here, with the same colour coding. The 2018 May spectrum (magenta) was acquired before the 2019 eruption. The spectra have been normalised to the same continuum, for ease of comparison. The blue dot denotes telluric emission. Bottom left: 2018 May 16 spectrum in the region of the Na I D lines, plotted in velocity space. The systemic velocity (–94 km s^{-1}; Mikołajewska et al. 2021) is shown by the dashed line. The blue dot denotes telluric emission. See text for discussion. Bottom right: permitted lines of He I 5875Å, 6678Å, and the forbidden O III 5006Å line before the 2019 eruption; compare with the middle panel of Fig. 9.

5.3 The *Spitzer* IRS spectrum

5.3.1 Emission lines

While there were strong emission lines (including coronal, fine structure and recombination) in the IRS spectrum of RS Oph, in data taken *after* its 2006 eruption (Evans et al. 2007a,b), there are no emission lines in the *Spitzer* IRS spectrum of the RN T CrB in quiescence (Evans et al. 2019).

A segment of the *Spitzer* IRS spectrum of V3890 Sgr, obtained in 2007 October, is shown in Fig. 10. It shows marginal evidence for two emission lines, namely the [Ne II] 12.813 μm (flux 8.4[$\pm$2.3] $\times$ 10^{-18} W m^{-2}) and [Ne III] 15.555 μm (flux 8.1[$\pm$2.3] $\times$ 10^{-18} W m^{-2}) fine structure lines. The flux ratio is

$$\frac{f([\mathrm{Ne\,II}])}{f([\mathrm{Ne\,III}])} \simeq 1.0 \pm 0.2 \ .$$

We assume that the upper levels of the Ne transitions are excited by electron collision. We take the effective collision strengths from the Iron Project[4] (Badnell et al. 2006), and the ionisation equilibrium data for neon from Arnaud & Rothenflug (1985). We determine the temperature of the gas in which the neon lines originate by an iterative process, and find that T(Ne) $\simeq$ 6.3 $\times$ 10^4 K. This does not seem unreasonable for a gas that is ionised by a WD and an AD.

There is no clear evidence for the presence of the [O IV] fine structure line at 25.89 μm (ubiquitous in CNe; Helton et al. 2012), and present in the spectrum of RS Oph (Evans et al. 2007a,b), to a 3σ upper limit of 3.7 $\times$ 10^{-18} W m^{-2}. At 10^4 K, the critical electron density above which the upper level of the [O IV] 25.89 μm line is collisionally de-excited is 9.9 $\times$ 10^3 cm^{-3}, implying that the electron density in the gas from which the [O IV] line would originate in the environment of V3890 Sgr exceeds this value.

5.3.2 The SED

In Section 5.1.1 we found $T_{\rm eff}$ = 3050 $\pm$ 200 K from fitting the NIR data. There were no NIR observations of V3890 Sgr at the time of the Spitzer observation so we have no value for $T_{\rm eff}$. However, as this spectral region is on the Rayleigh-Jeans tail of the RG's photospheric emission, the fit is not sensitive to $T_{\rm eff}$. However the abundances ([C] = +0.2, [Na] = +1.0, [Si] = +0.0) we determined in the fits to the NIR data will be the same at the time of the Spitzer observations and we adopt these here. We again assume $\log g = 0.7$, but explore different values of $T_{\rm eff}$.

[4] http://cdsweb.u-strasbg.fr/tipbase/home.html

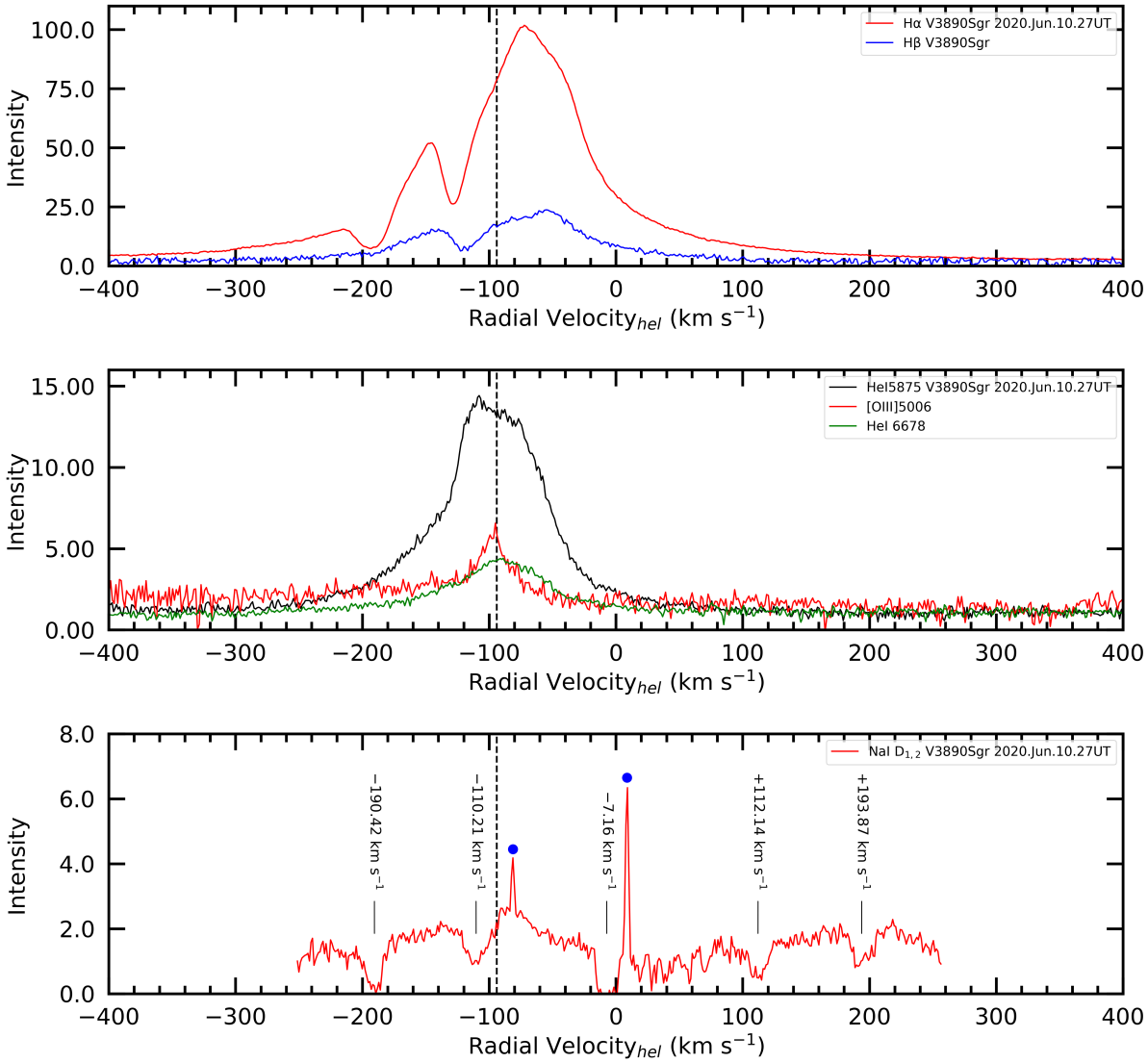

Figure 9. The PEPSI ($R = 130,000$) observed velocity profiles of various strong emission lines in V3890 Sgr post the 2019 RN eruption at a phase of 0.709. Top: Hα and Hβ. Middle: Permitted lines of He I 5875Å, 6678Å, and the forbidden O III 5006Å line. Bottom: The region of the Na I D lines, for which the velocities are calculated with respect to the D_2 line (5889.995Å air). The two narrow features marked by the blue circles are night sky sodium lines. Velocity components of various absorption features are indicated. Note that there are only three distinct Na I D absorption systems: the features at $-110.21\,\mathrm{km\,s^{-1}}$ and $-190.47\,\mathrm{km\,s^{-1}}$ are from the same systems as those at $+112\,\mathrm{km\,s^{-1}}$ and $+193\,\mathrm{km\,s^{-1}}$, but for D_1. The spectra are not absolutely flux calibrated, but are presented in continuum normalised intensity. These data have not been dereddened. The dashed vertical line in all the panels is the systemic velocity of the binary system, taken as $-94\,\mathrm{km\,s^{-1}}$ (Mikołajewska et al. 2021).

Around $T_{\rm eff} = 3000 - 3100$ K (close to the value we deduced for the NIR), the water bands are too strong. They may be decreased by further increasing [C] to +0.25, but this is not an option as this strongly affects the SED in the NIR (see Fig. 5 for the effect of the water bands): the C abundance is constrained by our fit to the NIR data. The alternative is to increase $T_{\rm eff}$, because at $T_{\rm eff} = 3300$ K the water bands disappear completely.

The fit to the IRS spectrum of V3890 Sgr is shown in the left panel of Fig. 11, in which an excess flux relative

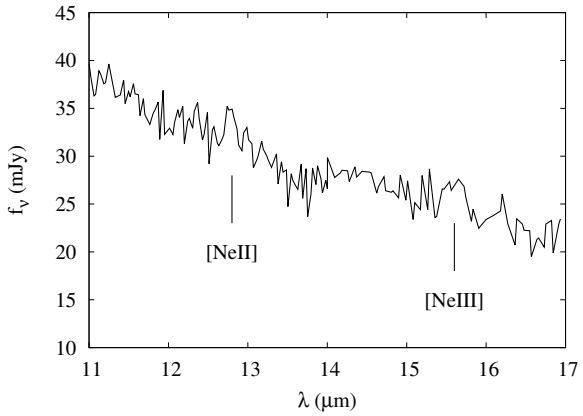

Figure 10. Possible detection of neon fine structure lines in the *Spitzer* IRS spectrum of V3890 Sgr.

to the RG photosphere (red curve) is evident longward of 7 μm. This additional flux is most plausibly provided by a dusty envelope around the RG, as reported by Rushton et al. (2010, 2014, 2022) for the case of RS Oph. However in the case of RS Oph, the dust shows strong silicate emission (Evans et al. 2007b; Woodward et al. 2008; Rushton et al. 2022), which is not present in V3890 Sgr. We follow the scheme of Rushton et al. and add a contribution from the dust, with temperature $T_{\rm dust}$ = 400 K, to the photospheric flux ($T_{\rm eff}$ = 3300 K). The additional blackbody emission greatly improves the fit, as shown by the blue curve in the left panel of Fig. 11.

We find that the model spectrum with $T_{\rm eff}$ = 3400 K resembles that for $T_{\rm eff}$ = 3300 K, but for this case $T_{\rm dust}$ = 450 K: there is some "degeneracy" in the $T_{\rm eff}$ and $T_{\rm dust}$ values. For example, we have the same fit for a 3400 K:450 K photosphere/dust temperature mix as we do for 3300 K:400 K, etc. However higher dust temperatures provide a greater contribution at shorter wavelengths. The fact that we see no evidence for dust in the NIR data sets limits on $T_{\rm dust}$ and $T_{\rm eff}$.

The value of $T_{\rm eff}$ required to fit the Spitzer data is somewhat higher than that obtained from fitting the NIR data (3050 K). The absence of the water bands, and the requirement that the carbon abundance must be +0.2 dex to fit the NIR data, limits $T_{\rm eff}$ at the low end to 3300 K. On the other hand, there is no evidence for dust in the NIR data, limiting $T_{\rm eff}$ to 3400 K at high end. Thus, despite the fact that the SED is not sensitive to $T_{\rm eff}$ in the Spitzer spectral range, our value of $T_{\rm eff}$ is quite robust. Noting that the Spitzer data were obtained when WD was in front of the RG, while all the NIR data were taken at quadrature, it is likely that we see real changes in temperature (see Section 3.1). A similar effect was found in our analysis of RS Oph (Pavlenko et al. 2016), in which the overall effect of irradiation was to increase $T_{\rm eff}$ by 100–200 K.

5.3.3 The SiO fundamental band

The presence of the SiO fundamental band near 8 μm in the spectrum of T CrB was reported by Evans et al. (2019). The Spitzer IRS spectrum of V3890 Sgr, shown in Fig. 11, resembles that of T CrB in that there is no 9.7 μm silicate emission feature (as there is in the case of the RN RS Oph; Evans et al. 2007b; Woodward et al. 2008; Rushton et al. 2014, 2022) but there is weak absorption in the SiO fundamental. As in the case of T CrB, this likely arises in the RG photosphere (Evans et al. 2022a).

The lines of the various SiO isotopologue fundamental transitions are strongly blended, and the resolution of the Spitzer IRS data is too low to identify the individual features. In general, including the higher mass isotoplogues provides a stronger 8 μm SiO band. We have no information about the Si isotopic ratios in V3890 Sgr: high resolution spectroscopy in the 4 μm first overtone is required to robustly determine the Si abundance ratios. We have therefore computed synthetic spectra on the assumption of solar Si isotopic abundances. As in case of modeling the IRS SED, the SiO fundamental band shows a weak dependence on the adopted $T_{\rm eff}$ in our temperature range.

The fit to the SiO fundamental is shown in Fig. 11. At $T_{\rm eff}$ = 3300 K, the 8 μm band is somewhat weaker than it is at 3100 K, but still stronger than it is in the observed spectrum.

The properties of the circumstellar dust, and of the absorptions in the SiO fundamental transition, are summarised in Table 4; note that, in Evans et al. (2019), the fit to the SiO fundamental was incorrect; see erratum in Evans et al. (2022a).

6 CONCLUSIONS

We have presented optical and infrared spectroscopy of the recurrent nova V3890 Sgr, covering the wavelength range 4070Å–38 μm. We find that

(i) the surface gravity of the red giant component is $\log g = 0.72 \pm 0.02$, and its effective temperature is in the range $T_{\rm eff}$ = 3050±200 K to $T_{\rm eff}$ = 3300±200 K;

(ii) there is an overabundance of both carbon (0.2 dex) and sodium (1 dex) relative to the solar value;

(iii) the ^{12}C/^{13}C ratio = 25 ± 2, a value similar to that found in red giants in other recurrent novae;

(iv) the interpretation of the quiescent spectrum in the 5–38 μm region requires the presence of photospheric SiO absorption and of cool ($\sim$ 400 K) dust in the red giant environment;

(v) the region of the Na I D lines includes a number of interstellar components. There is also evidence for interaction between ejecta from the 2019 eruption and material accumulated in the plane of the binary.

(vi) there is evidence for two neon fine structure lines, namely [Ne II] 12.813 μm and [Ne III] 15.555 μm, the flux ratio of which implies an electron temperature of 6.3×10^4 K;

(vii) the three RG in RN systems we have considered thus far have in common an overabundance of carbon and similar ^{12}C/^{13}C ratios; both properties are typical of RG photospheres after first dredge-up in stars of low initial mass. All three also have photospheric SiO in absorption.

ACKNOWLEDGMENTS

We thank the referee for their helpful and supportive comments.

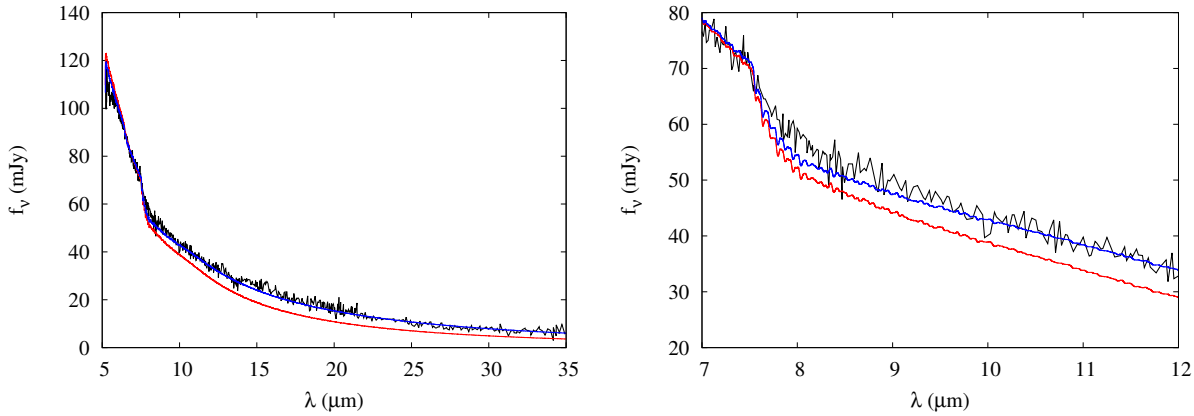

Figure 11. Left: Fit to the *Spitzer* IRS spectrum in the 5–35 μm region with a $T_{\rm eff} = 3300$ K, $\log g = 0.7$ photosphere. Black: V3890 Sgr, Red: $T_{\rm eff} = 3300$ K, $\log g = 0.7$ photosphere, and solar Si isotopic ratios. Blue: as red but including dust at $T = 400$ K. Right: Detail of fit in the 7–12 μm region; colour coding as left. See text for details.

AE thanks John Southworth for a helpful discussion on the orbital phase.

This study was funded as part of the routine financing programme for institutes of the National Academy of Sciences of Ukraine. YP gratefully acknowledges the hospitality of the Nicolaus Copernicus Astronomical Center, Toruń, and support from grant 2017/27/B/ST9/01128 financed by the Polish National Science Center, while this work was being completed. DPKB is supported by a CSIR Emeritus Scientist grant-in-aid and is being hosted by the Physical Research Laboratory, Ahmedabad. RDG was supported by the National Aeronautics and Space Administration (NASA) and the United States Air Force (USAF). FMW acknowledges support of the US taxpayers through NSF grant 1611443.

The work is based in part on archival data obtained using the Infrared Telescope Facility operated by the University of Hawaii under a cooperative agreement with NASA.

Data for this paper were obtained under IRTF programme 2020A-010. The Infrared Telescope Facility is operated by the University of Hawaii under contract 80HGTR19D0030 with the National Aeronautics and Space Administration.

Access to the SMARTS partnership is made possible in part by research support from Stony Brook University.

The LBT is an international collaboration among institutions in the United States, Italy and Germany. LBT Corporation partners are: The University of Arizona on behalf of the Arizona university system; Istituto Nazionale di Astrofisica, Italy; LBT Beteiligungsgesellschaft, Germany, representing the Max-Planck Society, the Astrophysical Institute Potsdam, and Heidelberg University; The Ohio State University, The University of Notre Dame, University of Minnesota and University of Virginia.

The authors would like to thank the SAO/NASA ADS team for the development and support of this system.

DATA AVAILABILITY

The data used in this paper are available in the various observatory archives, as follows:

(i) Spitzer: https://cassis.sirtf.com/atlas/

(ii) WISE: http://wise.ssl.berkeley.edu/

(iii) SMARTS: http://www.astro.sunysb.edu/fwalter/SMARTS/NovaAtlas/

(iv) PEPSI: The PEPSI data underlying this paper will be shared on a reasonable request to the corresponding author.

(v) IRTF: http://irtfweb.ifa.hawaii.edu/research/irtf_data_archive.php;

REFERENCES

Anupama G. C., Mikołajewska J., 1999, A&A, 344, 177
Anupama G. C., 2008, in RS Ophiuchi (2006) and the Recurrent Nova Phenomenon, Astronomical Society of the Pacific Conference Series, vol. 401, p. 31, San Francisco
Arnaud M., Rothenflug R., 1985, A&AS, 60, 425
Asplund M., Grevesse N., Sauval A. J., Scott P., 2009, ARAA, 47, 481
Badnell N. R., et al., 2006, in Planetary Nebulae in our Galaxy and Beyond, Proceedings of IAU Symposium 234, eds M. J. Barlow & R. H. Méndez, Cambridge University Press, Cambridge, p. 211
Booth R. A., Mohamed S., Podsiadlowski Ph., 2016, MNRAS, 457, 822
Cardelli J. A., Clayton G. C., Mathis J. S., 1989, ApJ, 345 245
Darnley M. J., Ribeiro V. A. R. M., Bode M. F., Hounsell R. A., Williams R. P., 2012, ApJ, 746, 61
Della Valle M., Izzo L., 2020, A&A Review, 28, 3
Evans A. et al., 2007a, ApJ, 663, L29
Evans A. et al., 2007b, ApJ, 671, L157
Evans A., Bode M. F., O'Brien T. J., Darnley M. J., 2008, eds, RS Ophiuchi (2006) and the Recurrent Nova Phenomenon, Astronomical Society of the Pacific Conference Series, Vol. 401, San Francisco
Evans A., Gehrz R. D., Woodward C. E., Helton L. A., 2014, MNRAS, 486, 3498
Evans A., et al., 2019, MNRAS, 486, 3498
Evans A., et al., 2022a, MNRAS, 512, 56
Evans A., et al., 2022b, MNRAS, submitted
Gehrz R. D., et al., 2007, Rev. Sci. Inst., 78, 011302
Harrison T. E., Johnson J. J., Spyromilio J., 1993, AJ, 105, 320
Helton L. A., et al., 2012, ApJ, 755, 37
Hill J. M., et al., 2012, SPIE, 8444, 84441A.
Houck J. R., et al., 2004, ApJS, 154, 18
Karakas A., Lattanzio J. J., 2014, PASA, 31, e030
Lebouteiller V., Barry D.J., Spoon H. W. W., Bernard-Salas J., Sloan G. C., Houck J. R., Weedman D., 2011, ApJS, 196, 8
Mikołajewska J., Iłkiewicz K., Gałan C., Monard B., Otulakowska-Hypka M., Sgara M. M., Udalski A., 2021, MNRAS, 504, 2122
Munari U., Walter F. M., 2019, ATel 13069
Page K. L., et al., 2020, MNRAS, 499, 4831
Pagnotta A., Schaefer B. E., 2014, ApJ, 788, 164
Pavlenko Ya. V., 2003, Astronomy Reports, 47, 59
Pavlenko Ya. V., 2013, Ap&SS, 279, 91
Pavlenko Ya. V., 2014, Astronomy Reports, 58, 825
Pavlenko Ya. V., Woodward C. E., Rushton M. T., Kaminsky B., Evans A., 2010, MNRAS, 404, 206
Pavlenko Ya. V., Kaminsky B., Rushton M. T., Evans A., Woodward C. E., Helton L. A., O'Brien T. J., Jones D., Elkin V., 2016, MNRAS, 456, 191
Pavlenko Y. V., Yurchenko S. N., Tennyson J., 2020a, A&A, 633, A52
Pavlenko Y. V., Evans A., Banerjee D. P. K., Geballe T. R., Munari U., Gehrz R. D., Woodward C. E., Starrfield S., 2020b, MNRAS, 498, 4853
Pereira A., 2019, VSNET-ALERT 23506
Perlmutter S., et al., 1999, ApJ, 517, 565
Prévot M. L., Lequeux J., Maurice E., Prévot L., Rocca-Volmerange B., 1984, A&A, 132, 389
Quiroga C., Mikołajewska J., Brandi E., Ferrer O., García L., 2002, A&A, 387, 139
Rayner J. T., Toomey D. W., Onaka P. M., Denault A. J., Stahlberger W. E., Vacca W. D., Cushing M. C., Wang, S., 2003, PASP, 115, 362
Rayner J. T., Cushing M. C., Vacca W. D., 2009, ApJS, 185, 289
Reiss A. G., et al., 1998, AJ, 116, 1009
Rushton M. T., et al., 2010, MNRAS, 401, 99
Rushton M. T., et al., 2014, in Woudt P. A., Riberio V. A. R. M., eds, ASP Conf. Ser. Vol. 490, Stella Novae: Past and Future Decades. Astron. Soc. Pac., San Francisco, p. 249
Rushton M. T., Woodward C. E., Gehrz R. D., Evans A., Kaminsky B., Pavlenko Ya. V., Eyres S. P. S., 2022, MNRAS, submitted
Schaefer B. E., 2009, ApJ, 697, 721
Schaefer B. E., 2010, ApJS, 187, 275
Soszynski, I., et al., 2013, AcA, 63, 21
Starrfield S., Iliadis C., Hix W. R., Timmes F. X., Sparks W M., 2009 ApJ, 692, 1532
Starrfield S., Iliadis C., Hix W. R., 2016, PASP, 128, 051001
Starrfield S., Bose M., Iliadis C., Hix W. R., Woodward C. E., Wagner R. M., 2020, ApJ, 895, 70
Strassmeier K. G., et al., 2015, AN, 336, 324
Unsöld A., 1927, Z. Phys., 43, 563
van Belle G. T., et al., 2021, ApJ, 922, 163
Werner M. W., et al., 2004, ApJS, 154, 1
Walter F. M., Battisti A., Towers S. E., Bond H. E., Stringfellow G. S., 2012, PASP, 124, 1057
Williams R. E., Hamuy M., Phillips M. M., Heathcote S. R., Wells L., Navarette M., 1991, ApJ, 376, 721
Williams R. E., Mason E, Della Valle M., Ederoclite A., 2008, ApJ, 685, 451
Woodward C. E. et al., 2008, in Evans A., Bode M. F., OBrien T. J., Darnley M. J., eds, ASP Conf. Ser. Vol. 401, RS Ophiuchi (2006) and the Recurrent Nova Phenomenon. Astron. Soc. Pac., San Francisco, p. 260
Woodward C. E., Banerjee D. P. K., Evans A., 2019, ATel 13764
Wright E. L., et al., 2010, AJ, 140, 1868

This paper has been typeset from a TEX/ LATEX file prepared by the author.